Structural relaxations around Ti, Cr and Fe impurities in α-Al_2O_3 probed by x-ray absorption near-edge structure combined with first-principles calculations

2005 J. Phys.: Condens. Matter 17 5467

(http://iopscience.iop.org/0953-8984/17/36/003)

INSTITUTE OF PHYSICS PUBLISHING JOURNAL OF PHYSICS: CONDENSED MATTER

J. Phys.: Condens. Matter **17** (2005) 5467–5480 doi:10.1088/0953-8984/17/36/003

Structural relaxations around Ti, Cr and Fe impurities in α-Al_2O_3 probed by x-ray absorption near-edge structure combined with first-principles calculations

Emilie Gaudry[1], Delphine Cabaret[1], Philippe Sainctavit[1], Christian Brouder[1], Francesco Mauri[1], José Goulon[2] and Andrei Rogalev[2]

[1] Laboratoire de Minéralogie-Cristallographie, UMR CNRS 7590, Université Pierre et Marie Curie, case 115, 4 place Jussieu, F-75252 Paris Cedex 05, France
[2] European Synchrotron Radiation Facility BP 220, F-38043 Grenoble Cedex, France

E-mail: delphine.cabaret@impmc.jussieu.fr

Received 12 July 2005, in final form 3 August 2005
Published 26 August 2005
Online at stacks.iop.org/JPhysCM/17/5467

Abstract

We determine the structural relaxations around paramagnetic impurities (Ti, Cr, Fe) in corundum (α-Al_2O_3), by combining x-ray absorption near-edge structure (XANES) experiments and *ab initio* calculations. The structural relaxations are found to be very local. We then show that XANES is sensitive to small variations in interatomic distances within the coordination shell of the absorbing atom. The experiments were carried out on single crystals of ruby and sapphires. Linear dichroic signals are essential to characterize the geometry of the impurity site. The calculations were performed within a self-consistent 'non-muffin-tin' framework, that uses pseudopotentials, a plane-wave basis set, and the continued fraction for the absorption cross section.

(Some figures in this article are in colour only in the electronic version)

1. Introduction

The presence of impurities in a crystal can influence its mechanical, magnetic, semiconducting, superconducting, dielectric, spectroscopic, and transport properties. To cite just a few specific examples, impurities can improve the voltage hold-off capability of insulating materials [1], they are critical for the optical properties of most laser materials and gemstones, and they turned out to be the secret of ancient Damascus steel blades [2].

Still, the local crystallographic structure around impurities is unknown in most cases, although it is an essential piece of information to understand their influence on the physical properties of the host and to carry out *ab initio* simulations of these materials. This situation is due to the experimental and theoretical difficulties that are met in obtaining microscopic

information on impurity systems. From the theoretical point of view, quantum calculations of impurity systems are difficult since they require the use of large supercells. From the experimental point of view, impurity systems can only be measured with methods which can selectively probe certain atomic species. Among such methods, many of them, such as electronic paramagnetic resonance, give only indirect information on the position and nature of the atoms surrounding the impurity. Due to the advent of third-generation synchrotron radiation facilities, x-ray absorption spectroscopy (XAS) is now able to investigate impurities in solids.

The extended x-ray absorption fine structure (EXAFS) region of an XAS spectrum provides quantitative information about the short range organization around the absorbing atom (interatomic distances, coordination number). The x-ray absorption near-edge structure (XANES) region usually gives qualitative information about the atomic arrangement up to the medium range order. XANES is sensitive to the electronic structure (bonding) and probes the empty states of solids. In the case of dilute elements in single crystals, especially at the K edge of 3d transition elements, collecting EXAFS spectra with a good signal-to-noise ratio is a difficult task, because the intensity of diffraction peaks becomes much larger than the EXAFS signal. Taking the example of impurities in corundum α-Al_2O_3 [3], good EXAFS spectra could be collected for 10 000 wt ppm Cr^{3+} impurities, but the usable energy range obtained for 1500 wt ppm Fe^{3+} impurities was already quite limited, and the concentration of colouring impurities is often an order of magnitude lower than this. In such cases, XANES becomes a practical and valuable technique to get information about the local structure of the absorbing atom [4]. However, the analysis of the experimental XANES data is not straightforward because of the photoelectron multiple-scattering processes that occur in the near-edge region. *Ab initio* XANES simulations are then required to relate the experimental spectral features to the local geometry around the aborbing atom.

Recently, an efficient first-principles approach based on plane-wave pseudopotential formalism has been developed to calculate K-edge XANES spectra [5]. Here we apply this method to the K edge of substitutional paramagnetic impurities in aluminium oxide. More precisely, we investigate the structural modifications of the corundum crystal structure induced by the presence of substitutional Ti^{3+}, Cr^{3+}, or Fe^{3+}. This system is chosen because corundum containing transition metal impurities is important for laser applications and as gemstones. Colourless corundum (α-Al_2O_3) becomes red ruby, pink sapphire, or yellow sapphire when a small amount of Cr^{3+}, Ti^{3+}, or Fe^{3+} ions substitute for Al^{3+} ions, respectively [6, 7]. The colour of blue sapphire is due to the presence of (Fe–Ti) pairs in α-Al_2O_3.

For this investigation, polarized XANES spectra are measured and calculated. Corundum belongs to the trigonal Bravais lattice, the optical axis being parallel to the [111] direction of the trigonal unit cell (i.e. to the *c*-axis of the hexagonal cell). Corundum is then a dichroic compound in the electric dipole approximation. The dichroic signal is a direct signature of the departure of the impurity site from octahedral symmetry [3]. The full angular dependence of XANES doubles the experimental data with which the structural model can be compared. XANES calculations are performed from structural models resulting from *ab initio* energy minimization calculations. The agreement of our experimental and theoretical spectra demonstrates that precise structural information can be extracted from the angular-dependent XANES spectra, provided the electronic potential is accurately modelled.

The paper is organized as follows. Section 2 is dedicated to the methods, including the description of the samples (section 2.1), the x-ray absorption measurements (section 2.2) and the calculation frameworks (section 2.3). Section 3 is devoted to the results and discussion: we first present the results of the structural relaxation around the substitutional Ti^{3+}, Cr^{3+} and Fe^{3+} ions in α-Al_2O_3 (section 3.1); we then discuss the influence of the core-hole effects in

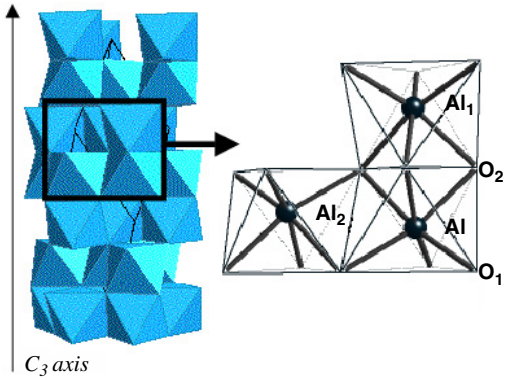

Figure 1. Aluminium atomic site in corundum. Left: the corundum structure is represented as a stacking of AlO_6 octahedra (the trigonal cell and the threefold symmetry axis are indicated). Right: zoom of the black-framed region of the left panel. The aluminium site with its O_1, O_2, Al_1 and Al_2 first four neighbours is indicated.

Table 1. Impurity concentration (in wt ppm) in the three doped α-Al_2O_3 samples.

Samples	Cr (wt ppm)	Fe (wt ppm)	Ti (wt ppm)
Red ruby	10 000 (±1000)	—	—
Blue sapphire	—	1500 (±50)	750 (±30)
Pink sapphire	—	—	540 (±30)

the case of the Cr K edge in ruby (section 3.2); and we finally compare calculated XANES spectra with experiments (section 3.3). Section 4 summarizes the conclusions of this study.

2. Methods

2.1. Crystallographic structure of α-Al_2O_3 and sample description

Corundum (α-Al_2O_3) belongs to the $R\bar{3}c$ (D^6_{3d}) space group [8]. The trigonal unit cell contains two Al_2O_3 formula units. The atomic environment of aluminium is illustrated in figure 1. The atomic site of aluminium is a distorted octahedron with a 3 (C_3) local point symmetry. The AlO_6 octahedron is characterized by two different Al–O interatomic distances. If we consider that the absorbing atom is denoted by Al in figure 1, the nearest three oxygen atoms are labelled O_1 in figure 1. The farther three oxygen atoms, labelled O_2, form a face shared by two octahedra along the threefold symmetry axis. Beyond the coordination shell of aluminium, the next two neighbours are aluminium atoms, labelled Al_1 and Al_2 in figure 1, and are relative to face-shared octahedra and edge-shared octahedra, respectively.

Three synthetic single crystals of doped α-Al_2O_3 (obtained by the Verneuil process) are used for this study: a red ruby (α-Al_2O_3:Cr^{3+}), a blue sapphire (α-Al_2O_3:Fe–Ti) and a pink sapphire (α-Al_2O_3:Ti^{3+}). The impurity concentration in each sample is given in table 1. They are measured with the Cameca Microbeam electron microprobe at the CAMPARIS analytical facility of Paris. A 30 kV acceleration with a 15 nA beam current, defocused to 10 μm, is used. X-ray intensities are corrected for dead-time, background, and matrix effects using the Cameca ZAF routine. The standards used are α-Al_2O_3, α-Cr_2O_3, α-Fe_2O_3 and TiO_2. The blue sapphire sample is chosen to represent the model compound of iron impurity in corundum (α-Al_2O_3:Fe^{3+}). It is indeed preferred to a yellow sapphire sample, that only contains

iron impurities, because synthetic yellow sapphires are known to be inhomogeneous [9]. Consequently, in this study, we assume that the low concentration of titanium (750 wt ppm) compared to that of iron (1500 wt ppm) does not affect the site relaxation around iron.

The samples are cylindrically shaped: 15 mm diameter and 3 mm thickness for the ruby sample, and 5 mm diameter and 1 mm thickness for the sapphire samples. They are cut so that the optical axis is in the plane of the disc surface, and the $[10\bar{1}]$ direction of the trigonal cell is orthogonal to the disc surface.

2.2. *X-ray absorption measurements*

X-ray absorption measurements are carried out at the European Synchrotron Radiation Facility (ESRF) on the ID12 beam line, which is dedicated to polarization dependent spectroscopies [10, 11]. The monochromatic x-ray beam is obtained through a double Si(111) crystal monochromator, with a resolution $\Delta E/E \simeq 10^{-4}$. The oriented samples are placed on a rotating holder with the normal of the disc surface parallel to the x-ray wavevector and to the rotation axis. The fluorescence intensity is measured by eight detectors symmetrically set around the x-ray beam.

XANES spectra are recorded for several angles θ between the optical axis of the sample and the x-ray polarization vector. We denote by $\sigma_{\parallel}$ and $\sigma_{\perp}$ the absorption cross section obtained with $\theta = 0°$ and 90°, respectively. In the electric dipole approximation, the isotropic signal is given by $(\sigma_{\parallel} + 2\sigma_{\perp})/3$, and the dichroic signal is given by the difference $\sigma_{\parallel} - \sigma_{\perp}$. The measurement of x-ray absorption spectra of impurities in crystals is impeded by the presence of large diffraction peaks. In order to decrease the intensity of diffraction peaks and elastic scattering, V and Mn filters (50 μm width) are used for the Cr K edge in ruby and the Fe K edge in blue sapphire, respectively. By so doing, the spectra recorded for the two angles $\theta = 0°$ and 90° are not affected by diffraction peaks. In contrast, no filter is available for the Ti K edge and the absorption was measured for 100 angles θ from 0 to 360°. The $\sigma_{\parallel}$ and $\sigma_{\perp}$ spectra are reconstructed from this amount of data by using a Fourier decomposition to remove the contribution of diffraction peaks to the spectra.

2.3. *Calculation methods*

The starting point of any XANES *ab initio* calculation is a structural model. The structural models for α-Al_2O_3:Ti^{3+}, α-Al_2O_3:Cr^{3+} and α-Al_2O_3:Fe^{3+} are obtained from the substitution in the corundum structure of one aluminium atom by one impurity Ti, Cr or Fe, respectively. These substituted structures are relaxed by *ab initio* energy minimization calculation, using Car–Parrinello molecular dynamics with simulated annealing [12] as implemented in the CPMD[3] code. The XANES calculations are then carried out within the scheme of the PARATEC[4] code, using the formalism described in [5]. Both codes are based on the density functional theory (DFT) within the spin polarized local density approximation (LSDA), and use a plane-wave basis set and norm-conserving Troullier–Martins pseudopotentials [13] in the Kleinman–Bylander form [14]. In the following, we give all the parameters used in both kinds of calculation.

[3] CPMD V3.7 Copyright IBM Corp 1990–2003, Copyright MPI für Festkörperforschung Stuttgart 1997–2001. For more information see http://www.cpmd.org.

[4] PARATEC is the Parallel Total Energy Code written by B Pfrommer, D Raczkowski, A Canning, and S G Louie, Lawrence Berkeley National Laboratory (with contributions from F Mauri, M Cote, Y Yoon, Ch Pickard, and P Haynes). For more information see www.nersc.gov/projects/paratec.

Table 2. Parametrization used for the generation of the pseudopotentials. The core radii of the valence states are indicated between parentheses in Å.

Atom	Al	O	Ti	Cr	Fe
Valence	3s (1.06)	2s (0.77)	3s (0.58)	3s (0.53)	3s (0.48)
states	3p (1.06)	2p (0.77)	3p (0.90)	3p (0.79)	3p (0.90)
	3d (1.06)		3d (0.90)	3d (0.79)	3d (0.90)
Local part	d	p	d	d	d

2.3.1. Structural model construction. The structural models are constructed from the lattice parameters and atomic positions resulting from a previous *ab initio* calculation, performed by Duan *et al* in α-Al_2O_3 [15, 16]. In [15], the trigonal unit cell parameters are $a_R = 5.11$ Å and $\alpha = 55.41°$, the aluminium atoms are in 4c symmetry sites with $x = 0.352$ and the oxygen atoms are in 6e symmetry sites[5] with $x = 0.555$. We verify by using CPMD that this corundum optimized structure obtained by Duan *et al* corresponds to atomic forces less than 2×10^{-3} Ryd Å^{-1}. Since we use periodic boundary conditions, we consider $2 \times 2 \times 2$ supercells. The supercells contain 80 atoms: 48 oxygen atoms, 31 aluminium atoms and one transition metal atom (Ti, Cr or Fe) in substitution for aluminium. With such large supercells, the interaction between two impurities (belonging to two neighbouring supercells) is negligible. All atoms are allowed to relax, while the lattice constants are fixed. The impurities considered in this study are known to be in a high-spin state [17], therefore the spin multiplet imposed on the trivalent impurities is $S = \frac{1}{2}$ for Ti^{3+} ($[Ar]4s^03d^1$), $S = \frac{3}{2}$ for Cr^{3+} ($[Ar]4s^03d^3$), and $S = \frac{5}{2}$ for Fe^{3+} ($[Ar]4s^03d^5$). The parametrization of the norm-conserving Troullier–Martins pseudopotentials is given in table 2. The wavefunctions and the charge density were expanded in plane waves with cut-off of 80 and 320 Ryd, respectively. Since the supercell is rather large, and since the systems are insulating materials, the Brillouin zone is only sampled at the Γ point.

2.3.2. XANES calculations. The method used for XANES calculations is described in [5, 18]. It uses periodic boundary conditions, a plane-wave basis set, pseudopotentials and reconstructs all-electron wavefunctions within the projector augmented wave (PAW) framework [19]. In order to allow the treatment of large supercells (hundreds of atoms), the scheme uses a recursion method to construct a Lanczos basis and then compute the cross section as a continued fraction [20, 21], in the electric dipole and quadrupole approximations[6]. Electric quadrupole transitions are relevant for the pre-edge region, in particular at the K edge of transition metals. The absorption cross section is calculated beyond the 'muffin-tin' approximation, that is known to limit the applications of the multiple scattering theory traditionally used for XANES simulations [22–24].

XANES spectra are computed at the transition metal K edge using the 80-atom supercells described in the previous subsection. The pseudopotentials were generated using the parametrization given in table 2. In order to take into account the core-hole effects in the calculations, the Ti, Cr and Fe pseudopotentials are obtained with only one 1s electron. The spin multiplet degeneracy is set by imposing the number of up and down states given by the CPMD code. Convergence of the XANES theoretical spectra is reached for the following set

[5] Within the $R\bar{3}c$ space group, the 4c symmetry site corresponds to the positions $\pm(x, x, x; x + \frac{1}{2}, x + \frac{1}{2}, x + \frac{1}{2})$ and the 6e symmetry site corresponds to the positions $\pm(x, \frac{1}{2} - x, \frac{1}{4}; \frac{1}{2} - x, \frac{1}{4}, x; \frac{1}{4}, x, \frac{1}{2} - x)$.

[6] For electric dipole and quadrupole transitions, the operator $\mathcal{O}$ of equation (2) in [5] is equal to $\hat{\varepsilon} \cdot \boldsymbol{r}$ and to $\frac{i}{2}\hat{\varepsilon} \cdot \boldsymbol{r}\boldsymbol{k} \cdot \boldsymbol{r}$, respectively. The unit vector $\hat{\varepsilon}$ is the direction of the polarisation of the incident photon beam, and $\boldsymbol{k}$ is the wavevector.

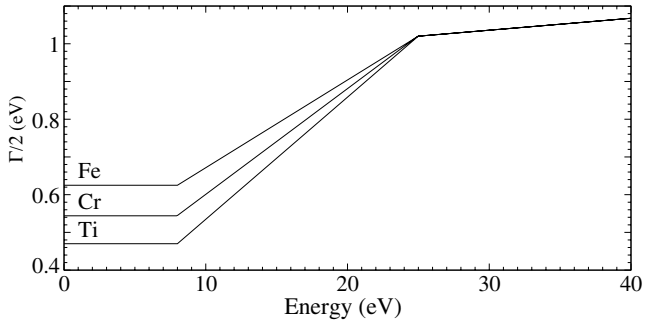

Figure 2. Energy dependence of the γ parameters used for the convolution of the XANES spectra at the Ti, Cr and Fe K edges in doped α-Al_2O_3. The zero in the energy scale refers to the highest occupied level in the corresponding structure.

of parameters: a 64 Ryd energy cut-off and one $\boldsymbol{k}$-point for the self-consistent spin-polarized charge density calculation, and 32 $\boldsymbol{k}$-points [25] for the absorption cross section calculation. An energy dependent broadening parameter γ is used in the continued fraction (see [5, 18]) in order to account for the two main photoelectron damping modes [26]. This width γ corresponds through the time–energy uncertainty relations to a lifetime of the photoelectron. At low energy, the lifetime of the photoelectron is only limited by the core-hole lifetime within the plasmon pole approximation. The parameter γ was then set to a constant, which corresponds to the K-level full width at half maximum given by Krause and Oliver [27]. At higher energy, the kinetic energy of the photoelectron is great enough that it can interact with the electron gas of the system. Its amplitude is damped, provoking a sharp decrease in the lifetime. Therefore, the γ parameter was set to rapidly increase, and then to have a smooth linear behaviour. The γ energy-dependent parameters used in this study are displayed in figure 2.

3. Results and discussion

3.1. Structural model analysis

The structural models of α-Al_2O_3:Cr^{3+} and α-Al_2O_3:Fe^{3+} have already been described and discussed in a previous work [3]. However, in order to compare with the structural model of α-Al_2O_3:Ti^{3+}, the main results of [3] are recalled here.

The analysis of the relaxation can only be done by careful comparison of the supercells before and after energy-minimization calculation. This is achieved by comparing *non-relaxed* and *relaxed* clusters, built from the supercells before and after energy-minimization calculation, respectively. The clusters are centred on the impurity and contain 66 atoms (5.2 Å radius). In order to avoid the influence of the impurity displacement in the *relaxed* model, we define the mass centre Ω of each cluster by calculating $\vec{O\Omega} = \sum_i m_i \vec{OM_i} / \sum_i m_i$, where O is the impurity position, M_i refers to all the atoms within a given cluster except the impurity and m_i is the mass of the atom i. For each atom i around the impurity, we evaluate the norm of the displacement vector, $\vec{V_i}$,

$$|\vec{V_i}|^2 = (X^i_{\text{relaxed}} - X^i_{\text{non-relaxed}})^2 + (Y^i_{\text{relaxed}} - Y^i_{\text{non-relaxed}})^2 + (Z^i_{\text{relaxed}} - Z^i_{\text{non-relaxed}})^2,$$

where $(X^i_{\text{non-relaxed}}, Y^i_{\text{non-relaxed}}, Z^i_{\text{non-relaxed}})$ and $(X^i_{\text{relaxed}}, Y^i_{\text{relaxed}}, Z^i_{\text{relaxed}})$ are the Cartesian coordinates of $\vec{\Omega M_i}$ vector in the *non-relaxed* and *relaxed* clusters, respectively. The angular relaxation was also determined. It was defined by the quantity $\delta\theta = \theta_{\text{non-relaxed}} - \theta_{\text{relaxed}}$,

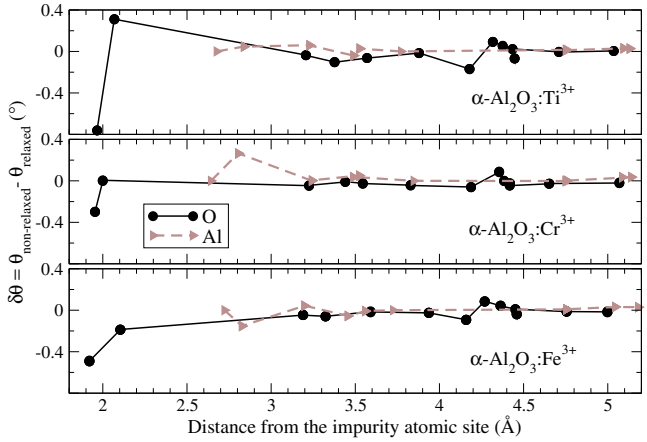

Figure 3. Angular relaxation around the paramagnetic impurities in doped α-Al_2O_3:$\delta\theta$ angle (see the text for explanation) as a function of distance from the impurity.

where θ_{relaxed} and $\theta_{\text{non-relaxed}}$ are the angles between the $\Omega\vec{M}_i$ directions and the C_3 axis in the *relaxed* and *non-relaxed* clusters, respectively. The comparison of the *relaxed* and *non-relaxed* clusters leads to the following conclusions.

First, the impurity site symmetry is conserved: the Ti, Cr and Fe atoms are still in a C_3 point symmetry site, characterized by two kinds of M–O_1 and M–O_2 distances (M = Ti, Cr or Fe). The angular relaxation is found to be very small (i.e. $<0.8°$). This is illustrated in figure 3, which gives $\delta\theta$ as a function of the distance between the impurity and its neighbouring atoms in the *relaxed* clusters.

Second, a displacement of the impurity from the initial aluminium site is observed in the three *relaxed* models. This displacement occurs along the C_3 axis, but its absolute value depends on the impurity. Chromium is displaced by 0.03 Å towards the Al_1 atom, titanium is displaced also by 0.03 Å but in the opposite direction, and iron is moved further (0.09 Å towards the Al_1 atom). The small displacement of chromium is in agreement with various experimental studies of the literature [28–32]. The result for iron is consistent with an analysis of electronic paramagnetic resonance (EPR) experiments, that gives a displacement of 0.04 ± 0.02 Å [33].

Third, an increase of distances within the coordination shell of the impurity is observed. This result is expected since the ionic radii of Ti, Cr and Fe in the octahedral site [34] ($r_{Ti^{3+}} = 0.670$ Å, $r_{Cr^{3+}} = 0.615$ Å and $r_{Fe^{3+}} = 0.645$ Å) are all greater than the ionic radius of aluminium ($r_{Al^{3+}} = 0.535$ Å). The calculated M–O_1 and M–O_2 bond lengths in doped α-Al_2O_3 were found to be close to M–O_1 and M–O_2 bond lengths in the corresponding metal oxides, α-M_2O_3 (α-Ti_2O_3, α-Cr_2O_3 and α-Fe_2O_3). In contrast, the distances M–Al_1 and M–Al_2 were less affected by the relaxation process: they are closer to Al–Al_1 and Al–Al_2 bond lengths in corundum than the M–M_1 and M–M_2 distances in the corresponding oxides α-M_2O_3. Table 3 gathers the M–O_1, M–O_2, M–Al_1 and M–Al_2 distances in α-Al_2O_3:M^{3+} deduced from the calculation, and compares them with the corresponding distances in α-Al_2O_3, α-Ti_2O_3, α-Cr_2O_3 and α-Fe_2O_3, resulting from x-ray diffraction experiments. One can remark in table 3 that the Ti–O_1 and Ti–O_2 bond lengths in α-Al_2O_3:Ti^{3+} (1.97 and 2.07 Å) are quite similar to those in α-Ti_2O_3 (2.01 and 2.07 Å). Besides, the Ti–Al_1 and Ti–Al_2 distances in α-Al_2O_3:Ti^{3+} (2.72 and 2.83 Å) are closer to the Al–Al_1 and Al–Al_2 distances in corundum (2.65 and 2.79 Å) than to the Ti–Ti_1 and Ti–Ti_2 distances in α-Ti_2O_3 (2.59 and 2.99 Å). One can notice that the experimental distances Cr–Cr_1 in α-Cr_2O_3 and Al–Al_1 in α-Al_2O_3 are both equal to 2.64 Å.

Table 3. M–O and M–Al bond lengths in α-Al_2O_3:M^{3+} (M = Ti, Cr, Fe) issued from the energy minimization calculations presented in section 3.1. These bond lengths are compared with the experimental and calculated Al–O and Al–Al interatomic distances in α-Al_2O_3 and to the M–O and M–M distances in α-M_2O_3.

		Interatomic distances (Å)			
Compound	Ref.	Cation–oxygen		Cation–cation	
α-Al_2O_3	[a]	$d_{Al-O_1} = 1.86$	$d_{Al-O_2} = 1.97$	$d_{Al-Al_1} = 2.65$	$d_{Al-Al_2} = 2.79$
α-Al_2O_3	[b]	$d_{Al-O_1} = 1.84$	$d_{Al-O_2} = 1.95$	$d_{Al-Al_1} = 2.62$	$d_{Al-Al_2} = 2.77$
α-Al_2O_3:Ti^{3+}	[c]	$d_{Ti-O_1} = 1.97$	$d_{Ti-O_2} = 2.07$	$d_{Ti-Al_1} = 2.72$	$d_{Ti-Al_2} = 2.83$
α-Al_2O_3:Cr^{3+}	[d]	$d_{Cr-O_1} = 1.95$	$d_{Cr-O_2} = 2.00$	$d_{Cr-Al_1} = 2.64$	$d_{Cr-Al_2} = 2.80$
α-Al_2O_3:Fe^{3+}	[d]	$d_{Fe-O_1} = 1.92$	$d_{Fe-O_2} = 2.10$	$d_{Fe-Al_1} = 2.72$	$d_{Fe-Al_2} = 2.83$
α-Ti_2O_3	[a]	$d_{Ti-O_1} = 2.01$	$d_{Ti-O_2} = 2.08$	$d_{Ti-Ti_1} = 2.59$	$d_{Ti-Ti_2} = 2.99$
α-Cr_2O_3	[e]	$d_{Cr-O_1} = 1.96$	$d_{Cr-O_2} = 2.01$	$d_{Cr-Cr_1} = 2.65$	$d_{Cr-Cr_2} = 2.88$
α-Fe_2O_3	[e]	$d_{Fe-O_1} = 1.94$	$d_{Fe-O_2} = 2.11$	$d_{Fe-Fe_1} = 2.90$	$d_{Fe-Fe_2} = 2.97$

[a] Experimental data from [8].
[b] Calculated data from [16].
[c] This calc.
[d] Calculated data from [3].
[e] Experimental data from [36].

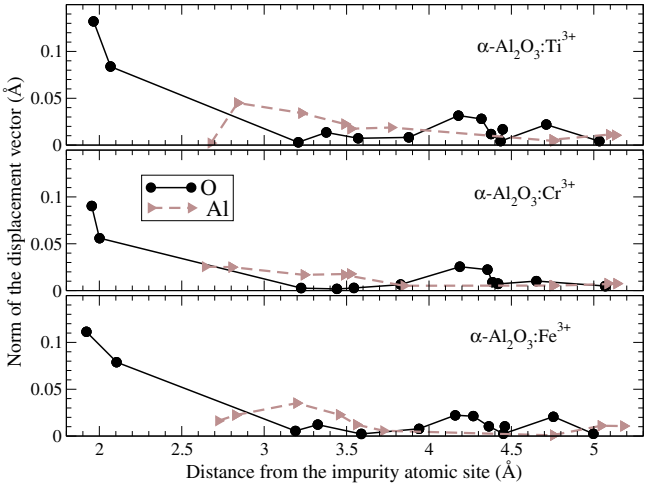

Figure 4. Radial relaxation around the paramagnetic impurities in doped α-Al_2O_3: norm of atomic displacement vectors (oxygen atoms in solid line with circles and aluminium atoms in dashed line with triangles) as a function of distance from the impurity.

Thus one expects that Cr–Al_1 distance in ruby (α-Al_2O_3:Cr^{3+}) should be around 2.64 Å. The calculated distances of α-Al_2O_3:Cr^{3+} are slightly larger (+0.015 Å) than those determined from EXAFS measurements on powder samples [32], and in good agreement (+0.005 Å) with EXAFS measurements performed on the same single crystal as the one used in the present study [3]. They are also consistent with data extracted from optical spectroscopy [35]. For α-Al_2O_3:Fe^{3+}, the calculated distances are in agreement with EXAFS experiments [3] and with EPR results [33].

Finally, the M–O and M–Al distances deduced from the *ab initio* relaxation calculations suggest that the structural relaxation around the transition metal impurities is almost local and mainly concerns the coordination shell. This point is confirmed by the calculations of the

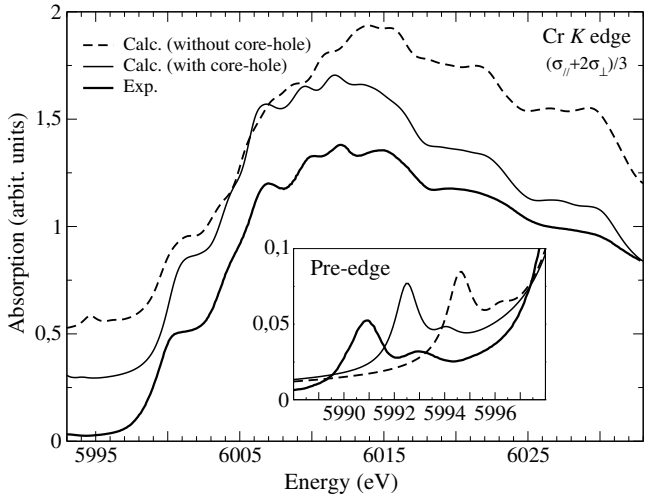

Figure 5. Influence of the core-hole effects in XANES calculation at the Cr K edge in ruby. Inset: zoom of the pre-edge region. For pre-edge simulations, the calculated spectra include both electric dipole and electric quadrupole transitions (the wavevector $\boldsymbol{k}$ is along the $[10\bar{1}]$ direction of the trigonal cell of ruby).

atomic displacements between the *relaxed* and *non-relaxed* clusters. Figure 4 represents the norm $|\vec{V}_i|$ as a function of the distance between the impurity and its neighbours in the *relaxed* model. It clearly shows that the oxygen coordination shell almost absorbs the relaxation. The displacement of atoms farther than 2.5 Å from the impurity is less than 0.035 Å. Comparing the three compounds, one also observes that the relaxation is slightly larger around titanium and iron than around chromium.

3.2. *Core-hole effects*

The influence of the core hole can be described by calculating a self-consistent potential around a core hole or by solving a Bethe–Salpeter equation [37, 38]. For impurity systems, solving a Bethe–Salpeter equation is probably beyond the reach of available computer programs. Moreover, it has already been observed that both methods give quite similar results [5]. Therefore, we shall describe the influence of the core hole by calculating a self-consistent potential in the presence of a 1s core hole. It is important to quantify the effect of the core hole because, when it is negligible [26], the XANES spectrum gives a direct picture of the empty p local density of states in the ground state.

Calculated spectra performed with or without the presence of a 1s core hole on the chromium absorbing atom are compared in figure 5. It clearly appears that the core hole is needed to obtain a good agreement with the experimental curve. In particular, the intensity and the energy positions of the features within the 6005–6017 eV energy range are not well reproduced if the core hole is not taken into account in the calculation. We have noticed similar behaviours due to the presence of the core hole at the titanium and iron K edges in α-Al_2O_3:Ti^{3+} and α-Al_2O_3:Fe^{3+}, respectively.

On the other hand, the presence of the core hole has a non-negligible impact in the pre-edge region. This is illustrated in the inset of figure 5, which represents the pre-edge region (5985–5998 eV) of the Cr K edge in α-Al_2O_3:Cr^{3+}. An interpretation of this region in terms of group theory has been detailed in [39]. In the pre-edge region both electric dipole ($1s \rightarrow p$) and quadrupole ($1s \rightarrow 3d$) transitions occur. Since the site of the impurity in doped α-Al_2O_3

is not centrosymmetric, the p states are present in the pre-edge through p–d hybridization. The calculated curves shown in the inset of figure 5 are the sum of both contributions. For the calculation of electric quadrupole transitions, the direction of the wavevector of the photon beam, $\boldsymbol{k}$, has to be specified. In the experiments, the single crystals were placed on the rotating holder so that the wavevector was parallel to the $[10\bar{1}]$ crystallographic direction. Consequently, the spectra $(\sigma_{\parallel} + 2\sigma_{\perp})/3$ shown in figure 5 are calculated with $\boldsymbol{k} \parallel [10\bar{1}]$.[7] The two features of the experimental pre-edge are reproduced with or without the 1s core hole (see the inset of figure 5). The presence of the core hole essentially provokes a 2.5 eV shift towards lower energy of the pre-edge features, while the main rising edge is not shifted. A similar energy shift due to the core hole was already observed for electric quadrupole transitions at the Ti K pre-edge in rutile [40]. Unfortunately, here the shift induced by the presence of the core hole is not large enough to give a perfect agreement with experiment. This problem may be due to the limit of the density functional theory within LDA to model the core hole–electron interaction for empty d states of 3d transition metals. LDA + U calculations could possibly improve the agreement in the pre-edge region. Indeed, in [41], the authors show that LDA + U calculations performed on ruby essentially affect the positions of Cr d and empty p levels.

3.3. Comparison between experimental and calculated XANES spectra

We first compare experimental spectra with each other. Figures 6(a)–(c) display $(\sigma_{\parallel} + 2\sigma_{\perp})/3$ and $\sigma_{\parallel} - \sigma_{\perp}$ signals recorded at the Ti K edge for the pink sapphire sample, at the Cr K edge for the ruby sample, and at the Fe K edge for the blue sapphire sample, respectively. One observes that the experimental spectra present comparable overall shapes. The Fe K edge seems to be less resolved than the Ti and Cr K edges, probably for the following two reasons:

(i) the core-hole lifetime is shorter at the Fe K edge (1.25 eV) than at the Cr K edge (1.08 eV) and at the Ti K edge (0.94 eV) [27];
(ii) the instrumental resolution is estimated to be 0.9 eV at the Fe K edge while it is 0.6–0.7 eV at both the Cr and Ti K edges.

There are also similarities between the M K edges (M = Ti, Cr, Fe) in α-Al_2O_3:M^{3+} and in α-M_2O_3 (see [42] for the Cr K edge in α-Cr_2O_3 and the Fe K edge in α-Fe_2O_3, and [43] for the Ti K edge in α-Ti_2O_3). At least to a certain extent, these spectra could be considered as the signature of a transition metal ion with a +III oxidation state in a sixfold coordinated environment. However, it is here necessary to perform calculations to go farther in the XANES analysis.

Figure 6 also compares experimental and theoretical XANES spectra. It can be seen that a good agreement is obtained: energy positions and relative intensities of the various features are well reproduced in each case. The agreement is especially good at the Ti K edge in pink sapphire and at the Cr K edge in ruby. It should be emphasized that not only the averaged $(\sigma_{\parallel} + 2\sigma_{\perp})/3$ spectra are correctly reproduced, but also the dichroic signal, from which more reliable structural information could be extracted. Such a good agreement with angular dependent spectra has also been obtained with the same calculation method: at the Al K edge in corundum [18] and at the Si K edge in α-quartz [5].

We have seen in section 3.1 that the relaxation around the impurity in the three compounds is local and essentially concerns the interatomic distances within the coordination shell of the impurity. Therefore, it is interesting to determine the sensitivity of XANES to such subtle structural modifications. Figure 7 compares $\sigma_{\parallel}$ and $\sigma_{\perp}$ experimental spectra with

[7] One should keep in mind that $(\sigma_{\parallel} + 2\sigma_{\perp})/3$ is the isotropic spectrum only in the electric dipole approximation, and under no circumstances in the electric quadrupole approximation.

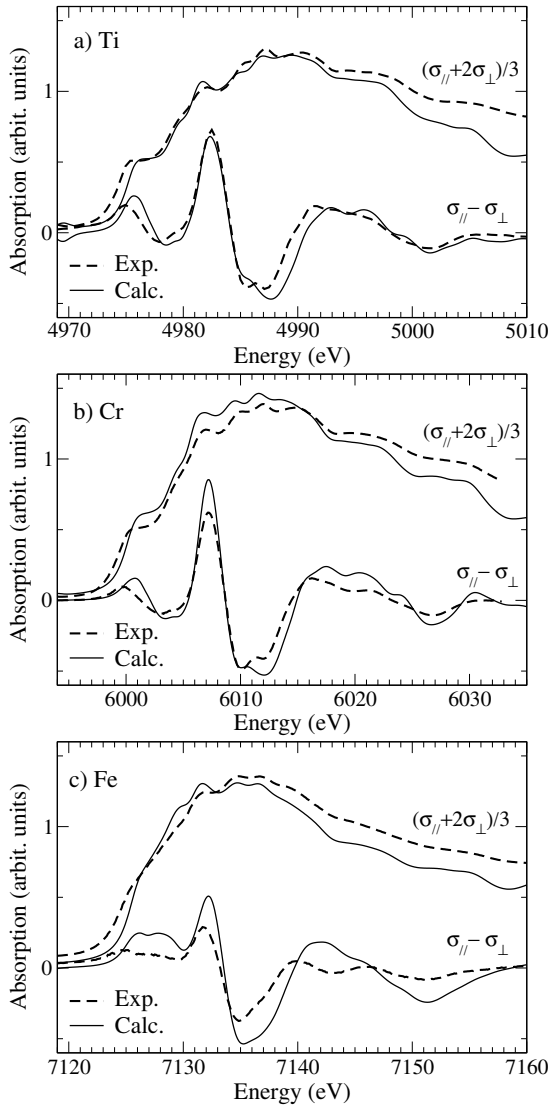

Figure 6. Comparison between experimental XANES data (dashed line) and calculated spectra (solid line): (a) the Ti K edge in pink sapphire (α-Al_2O_3:Ti^{3+}); (b) the Cr K edge in ruby (α-Al_2O_3:Cr^{3+}); (c) the Fe K edge in blue sapphire (α-Al_2O_3:Fe–Ti). An energy shift was added to the valence band maximum in the calculations in order to match with experiments: 4966 eV at the Ti K edge, 5991 eV at the Cr K edge and 7118 eV at the Fe K edge.

the corresponding calculated spectra carried out on the supercells before and after energy-minimization calculations, referred to as *non-relaxed* and *relaxed* calculations, respectively. First of all, it is worth noting that the differences observed between calculated spectra are small but not negligible. For all compounds, peaks labelled g in $\sigma_{\parallel}$ and labelled I and J in $\sigma_{\perp}$ are too strong in the *non-relaxed* calculated spectra. Consequently, these features (all located at about 30 eV above the edge) are clearly related to photoelectron scattering involving the first neighbours of the impurity. The same conclusion can be made for the shoulders labelled A and B in $\sigma_{\perp}$ and b in $\sigma_{\parallel}$. Especially at the Cr K edge in $\sigma_{\perp}$ signal, one can see that the double feature (D and E) is better reproduced by the *relaxed* calculation than by the *non-relaxed* one.

In the case of α-Al_2O_3:Cr^{3+}, the structural model is validated by our experimental EXAFS [3] and XANES data. In the case of α-Al_2O_3:Ti^{3+}, no EXAFS data were available but the structural model is validated by the excellent agreement with XANES experimental

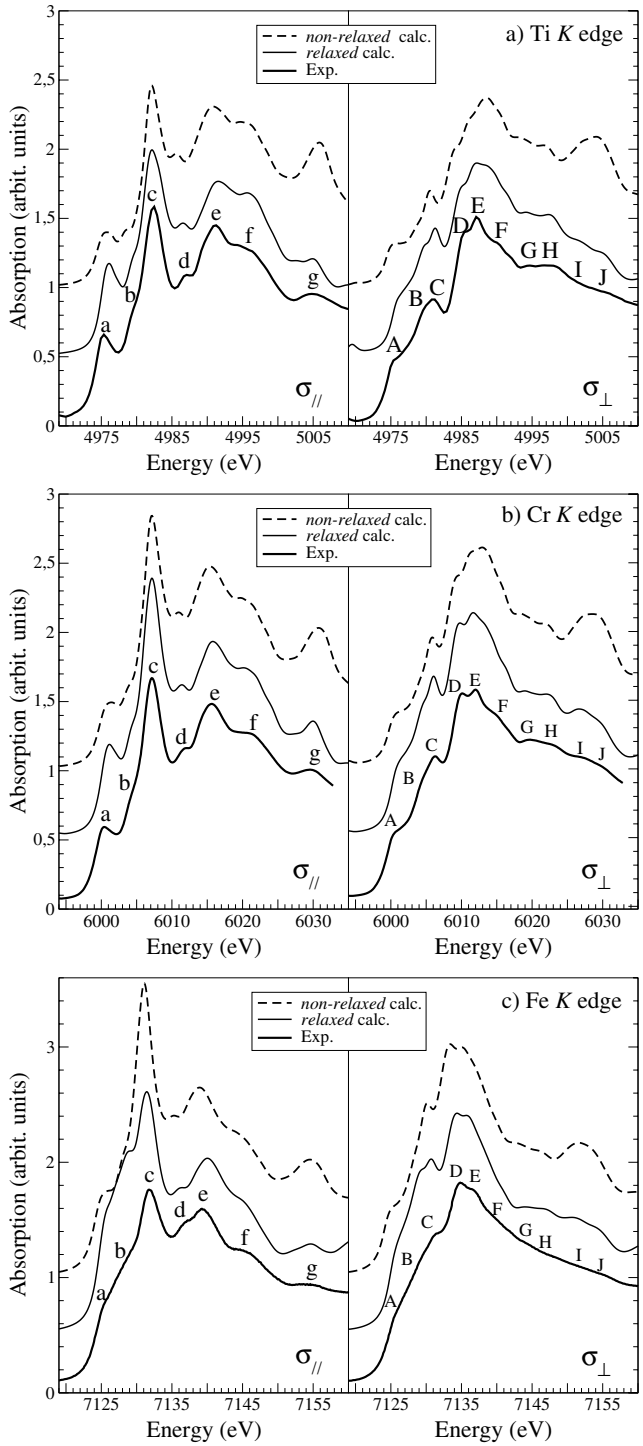

Figure 7. Comparison between $\sigma_{\parallel}$ (left) and $\sigma_{\perp}$ (right) experimental data (thick solid line) and theoretical spectra obtained with the supercells before (dashed line) and after (thin solid line) energy-minimization calculation: (a) the Ti K edge in pink sapphire, α-Al_2O_3:Ti^{3+}; (b) the Cr K edge in ruby, α-Al_2O_3:Cr^{3+}; (c) the Fe K edge in blue sapphire, α-Al_2O_3:Fe–Ti.

spectra. In the case of α-Al_2O_3:Fe^{3+}, the structural model is probably not fully satisfactory because the agreement with EXAFS [3] and XANES data is poorer.

4. Conclusions

In this paper, we have shown that XANES can provide valuable information about the small structural relaxation occurring within the atomic site of an impurity in an aluminium oxide matrix. This has been achieved by (i) measuring angular dependent XANES spectra in order to probe the distortion of the impurity site, (ii) calculating the structural model by *ab initio* energy minimization, (iii) calculating the XANES spectra from the previous theoretical structural models using the full-potential pseudopotential self-consistent method of [5]. The good agreement obtained between experimental and calculated spectra permits the validation of structural models. We have also pointed out the importance of the electronic potential construction to carry this study to a successful conclusion. Our work shows that detailed structural information can be extracted from XANES spectra, which is particularly relevant when good quality EXAFS measurements are difficult to collect, for example in the case of dilute samples. The structural data that we obtain can be used as a starting point for the calculation of important physical properties such as the optical spectra or the voltage hold-off capability.

Acknowledgment

We wish to acknowledge the computational support of the French Institut du Développement et de Recherche en Informatique Scientifique in Orsay, where all the calculations of this study were carried out.

References

[1] Miller H C 1981 *Physica* C **104** 183–8
[2] Verhoeven J D, Pendray A H and Dauksch W E 1998 *JOM* **50** 58–64
[3] Gaudry E, Kiratisin A, Sainctavit Ph, Brouder Ch, Mauri F, Ramos A, Rogalev A and Goulon J 2003 *Phys. Rev.* B **67** 094108:1–10
[4] Waychunas G A, Fuller C C, Davis J A and Rehr J J 2003 *Geochim. Cosmochim. Acta* **67** 1031–43
[5] Taillefumier M, Cabaret D, Flank A-M and Mauri F 2002 *Phys. Rev.* B **66** 195107
[6] Burns R G 1993 *Mineralogical Applications of Cristal Field Theory* (*Cambridge Topics in Mineral Physics and Chemistry* vol 5) 2nd edn (Cambridge: Cambridge University Press)
[7] Nassau K 1983 *The Physics and Chemistry of Color* (New York: Wiley–Interscience)
[8] Newnham R E and de Haan Y M 1962 *Z. Kristallogr.* **117** 235–7
[9] Eigenmann H K 1970 *PhD Thesis* Eidgenössischen Technischen Hochschule, Zürich
[10] Goulon J, Rogalev A, Gauthier C, Goulon-Ginet C, Paste S, Signorato R, Neumann C, Varga L and Malgrange C 1998 *J. Synchrotron Radiat.* **5** 232–8
[11] Rogalev A, Goulon J, Goulon-Ginet C and Malgrange C 2001 *Magnetism and Synchrotron Radiation* ed E Beaurepaire, F Scheurer, G Krill and J-P Kappler (Berlin: Springer)
[12] Car R and Parrinello M 1985 *Phys. Rev. Lett.* **55** 2471–4
[13] Troullier N and Martins J L 1991 *Phys. Rev.* B **43** 1993–2006
[14] Kleinman L and Bylander D M 1982 *Phys. Rev. Lett.* **48** 1425–8
[15] Duan W, Wentzcovitch R M and Thomson K T 1998 *Phys. Rev.* B **57** 10363–9
[16] Duan W, Paiva G, Wentzcovitch R M and Fazzio A 1998 *Phys. Rev. Lett.* **81** 3267–70
[17] Lever A B P 1984 *Inorganic Electronic Spectroscopy* (Amsterdam: Elsevier)
[18] Cabaret D, Gaudry E, Taillefumier M, Sainctavit Ph and Mauri F 2005 *Phys. Scr.* T **115** 131–3
[19] Blöchl P E 1994 *Phys. Rev.* B **50** 17953–79
[20] Haydock R, Heine V and Kelly M J 1972 *J. Phys. C: Solid State Phys.* **5** 2845–58
[21] Haydock R, Heine V and Kelly M J 1975 *J. Phys. C: Solid State Phys.* **8** 2591–605
[22] Ankudinov A L, Ravel B, Rehr J J and Conradson S D 1998 *Phys. Rev.* B **58** 7565–76
[23] Natoli C R, Misemer D K, Doniach S and Kutzler F W 1980 *Phys. Rev.* A **22** 1104–8
[24] Benfatto M, Della Longa S and Natoli C R 2003 *J. Synchrotron Radiat.* **10** 51–7
[25] Monkhorst H J and Pack J D 1976 *Phys. Rev.* B **13** 5188–92

[26] Kokubun J, Ishida K, Cabaret D, Mauri F, Vedrinskii R V, Kraizman V L, Novakovich A A, Ktivitskii E V and Dmitrienko V E 2004 *Phys. Rev.* B **69** 245103
[27] Krause M O and Oliver J H 1979 *J. Phys. Chem. Ref. Data* **8** 329–38
[28] Laurance N, McIrvine E C and Lambe J 1962 *J. Phys. Chem. Solids* **23** 515–31
[29] Lohr L L and Lipscomb W H 1963 *J. Chem. Phys.* **38** 1607–12
[30] Moss S C and Newnham R E 1964 *Z. Kristallogr.* **120** 359–63
[31] McCauley J W and Gibbs G V 1972 *Z. Kristallogr.* **135** 453–5
[32] Kizler P, He J, Clarke D R and Kenway P R 1996 *J. Am. Ceram. Soc.* **79** 3–11
[33] Zheng W-C 1998 *Physica* B **245** 119–22
[34] Shannon R D 1976 *Acta Crystallogr.* A **32** 751–67
[35] Langer K 2001 *Z. Kristallogr.* **216** 87–91
[36] Finger L W and Hazen R M 1980 *J. Appl. Phys.* **51** 5362–7
[37] Shirley E L 1998 *Phys. Rev. Lett.* **80** 794–7
[38] Soininen J A and Shirley E L 2001 *Phys. Rev.* B **64** 165112
[39] Gaudry E, Cabaret D, Sainctavit Ph, Brouder Ch, Mauri F, Rogalev A and Goulon J 2005 *Proc. XAFS-12 (Sweden, 2003)*; *Phys. Scr.* T **115** 191–3
[40] Joly Y, Cabaret D, Renevier H and Natoli C R 1999 *Phys. Rev. Lett.* **82** 2398–401
[41] Mazurenko V V, Varaksin A N, Mazurenko V G, Kortov V S and Anisimov V I 2004 *Physica* B **344** 385–90
[42] Grunes L A 1983 *Phys. Rev.* B **27** 2111–31
[43] Waychunas G A 1987 *Am. Mineral.* **72** 89–101